Engineering Analysis with Boundary Elements 122 (2021) 102–116

Contents lists available at ScienceDirect

Engineering Analysis with Boundary Elements

journal homepage: www.elsevier.com/locate/enganabound

# A dual interpolation boundary face method for 3D elasticity

Jianming Zhang [a,*], Chuanming Ju [a], Pihua Wen [b], Xiaomin Shu [a], Weicheng Lin [a], Baotao Chi [a]

[a] State Key Laboratory of Advanced Design and Manufacturing for Vehicle Body, College of Mechanical and Vehicle Engineering, Hunan University, Changsha 410082 China

[b] School of Engineering and Materials Science, Queen Mary University of London, London E1 4NS, UK

ARTICLE INFO

*Keywords:*
Dual interpolation boundary face method
3D elasticity
Boundary element method
Moving least-squares approximation

ABSTRACT

The dual interpolation boundary face method (DiBFM) proposed recently has been successfully applied to solve various problems in two dimensions. Compared with the conventional boundary element method (BEM), it has been proved that the DiBFM has the advantages of higher accuracy, convergence rate and computational efficiency. In addition, the DiBFM is suitable to unify the conforming and nonconforming elements in the BEM implementation, as well as to approximate both continuous and discontinuous fields. Moreover, there are no geometric errors by the DiBFM in the computational process. In this paper, the DiBFM is extended successfully to solve the elasticity problems in three-dimensions (3D) with formulations derived in details. A number of numerical examples are presented in order to validate the accuracy and convergence rate of the proposed method.

## 1. Introduction

The dual interpolation boundary face method has been successfully developed to solve various 2D problems including potential [1], elasticity [2], thin-walled structures [3], contact [4], and V-shaped notch problems [5]. Recently the DiBFM was also successfully applied to solve 3D potential problems [6]. This is due to the fact that the DiBFM can achieve higher accuracy and convergence rates than the conventional BEM for most cases [1]. These advantages stem from the fact that the DiBFM is coupled between the dual interpolation method and the boundary face method.

The dual interpolation method specifically refers to the first-layer interpolation and the second-layer interpolation, while the element in the method is called dual interpolation element. The dual interpolation element consists of source and virtual nodes, as shown in Fig. 1. When ignoring virtual nodes, it becomes a conventional discontinuous element. If both the virtual nodes and the source nodes are considered, then it amounts to a standard continuous element. In this manner, the continuous and discontinuous elements schemes can be unified by the dual interpolation element [1,7]. Thus, the geometric corner problems [2,8,9] and the mesh generation can be treated easily [10,11].

The first-layer interpolation is similar to the interpolation in a conventional continuous boundary element. Namely, both source nodes and virtual nodes in the dual interpolation elements are used for interpolation. By adding the virtual nodes in dual interpolation elements and comparing to the interpolation function order of the conventional discontinuous elements which use the source nodes only [1,4], the interpolation order of the dual interpolation elements is increased obviously. This results in a significant improvement for interpolation accuracy.

The second-layer interpolation is constructed by the moving least square (MLS) approximation and this approximation is employed to condense the degrees of freedom associated with virtual nodes, which do not act as collocation points in DiBFM [1,2]. Thus, only the variables associated with the source nodes form the unknowns in the final system equations and therefore the system matrix in the DiBFM is of the same size as the conventional BEM with the source nodes alone. Due to a significant improvement in interpolation accuracy, the DiBFM can achieve higher computational accuracy. Furthermore, the second-layer interpolation is of the ability to approximate both continuous and discontinuous fields accurately. Therefore, the continuous displacement and discontinuous tractions at the geometric corners or edges are treated easily.

The boundary face method (BFM) is also based on the boundary integral equation without introducing geometric errors [12], since BFM uses CAD geometries directly in its implementation. In addition, the BFM inherits the advantages of BEM including dimension reduction, higher accuracy and infinite domain problems without truncation or artificial boundary conditions [13]. These advantages are also inherited by DiBFM.

Due to the above advantages, DiBFM has been developed to various 2D problems [1-5]. However, the 2D model is a simplification from 3D problem and it is difficult to truly reflect the 3D practical problem. In order to demonstrate the advantages in solving practical problems, the DiBFM has been applied for 3D potential problems [6]. However, small features can cause significant stress concentration in 3D elasticity prob-

* Corresponding author.
*E-mail address:* zhangjianm@gmail.com (J. Zhang).

https://doi.org/10.1016/j.enganabound.2020.10.015
Received 27 May 2019; Received in revised form 13 January 2020; Accepted 21 October 2020
Available online 24 October 2020
0955-7997/

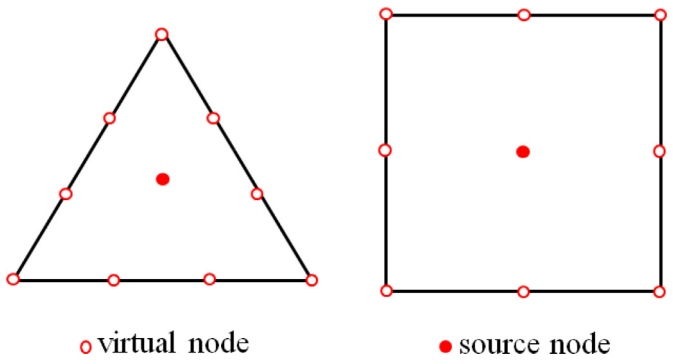


**Fig. 1.** Dual interpolation elements in 3D problems.

lems. Thus this paper firstly extends the DiBFM to 3D elasticity problems with the dual interpolation element. And it verifies the DiBFM has the ability to solve the problem of structure with a small feature. For 3D elasticity problems, a general formulation of the DiBFM is also derived in details. A potential advantage of the DiBFM compared with the BFM is briefly introduced in Section 2. Then the dual interpolation method for 3D problem is introduced in Section 3, and a general formulation of the elastic problems is presented in Section 4. Numerical examples are presented in Section 5. Finally, the conclusions and future work are given in Section 6.

## 2. Dual interpolation boundary face method

The DiBFM is coupled between the dual interpolation method and the boundary face method. In boundary face method, the integrand quantities, such as the coordinates of Gauss integration points, out normal and Jacobian, are calculated directly from the boundary faces, rather than from mesh elements. This is similar to the isogeometric BEM (IGABEM) in which NURBS are used to accurately represent structural geometry [14-17]. Thus, no geometric errors are introduced after discretization as shown in Fig. 2. More details can refer to the references [12,18,19].

Compared with the BFM, the DiBFM does not require geometric repair operations for the 'dirty' geometry model (see Fig. 3). The reason is explained as follows. Same as the BFM, the DiBFM has no continuity requirement for trial functions, and thus discontinuous grids can be used to discretize the CAD model. Due to the discontinuous grids allow to the existence of hanging points, discontinuous grids are more freedom for discretizing "dirty" geometry without geometry repair than continuous grids (see Fig. 4). However, the grids in 'bad' shape often appear in the discretization results of geometric models, especially in 'dirty' geometry models without geometric repair (slender quadrilateral grid shown in

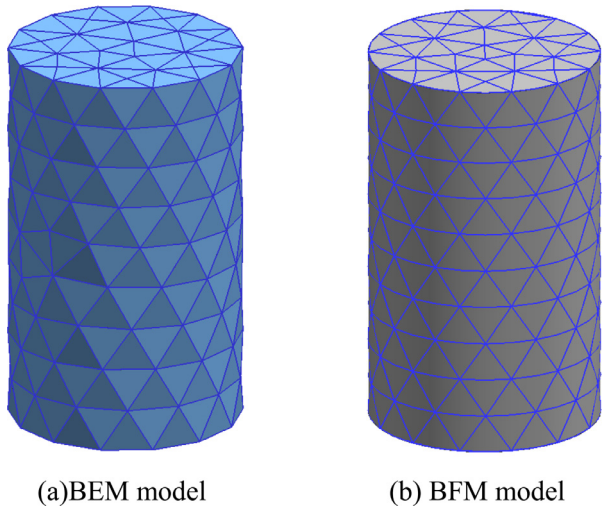


**Fig. 2.** Discrete model by different methods.

Fig. 4). Different from the BFM, the DiBFM improves the interpolation order of discontinuous element (see Fig. 5), resulting in the potential advantages that the DiBFM reduces the requirement of shape regularity for elements. Thus the DiBFM has the potential ability to analyze a "dirty" geometry model discretized by discontinuous grids. And this is our future work.

In addition, the binary-tree subdivision method (BTSM) [20] is applied in the implementation of the DiBFM to evaluate the singular integrals. Even if the shape of an element is irregular, the BTSM can also evaluate singular integrals accurately and efficiently [20]. A simple description of the BTSM is presented in Section 4.

## 3. Dual interpolation method in the DiBFM

### 3.1. The element in DiBFM

In DiBFM, the elements, called as dual interpolation elements, consist of source and virtual nodes as shown in Figs. 6 and 7 for triangular and quadrilateral elements respectively. Though the dual interpolation elements have been mentioned in [6], it is necessary to repeat them here to ensure the integrity of our paper.

As shown in Figs. 6 and 7, all nodes in a dual interpolation element are classified into two groups: (1) all source nodes are located inside the element, and (2) all virtual nodes are located on the edges and vertexes of the element. If the virtual nodes are removed, the dual interpolation element becomes a conventional discontinuous element. If both the vir-

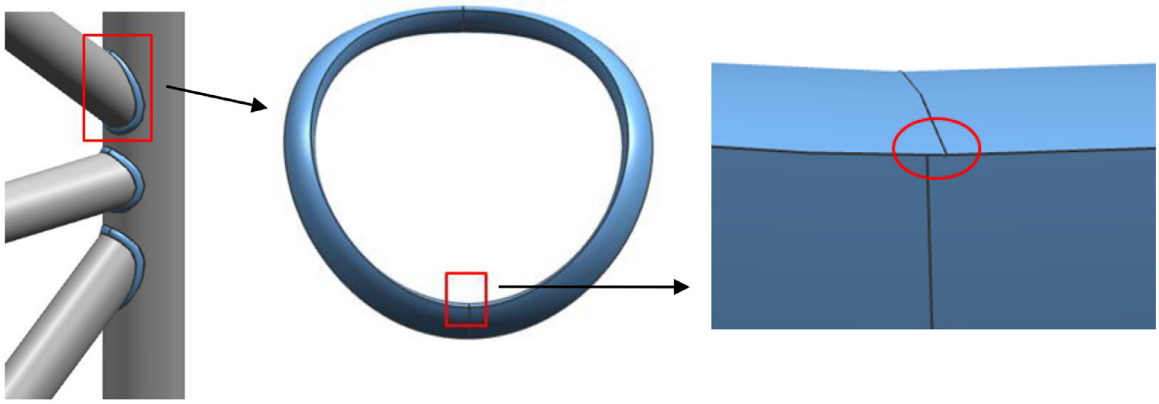

**Fig. 3.** Steel frame weld with short edge.

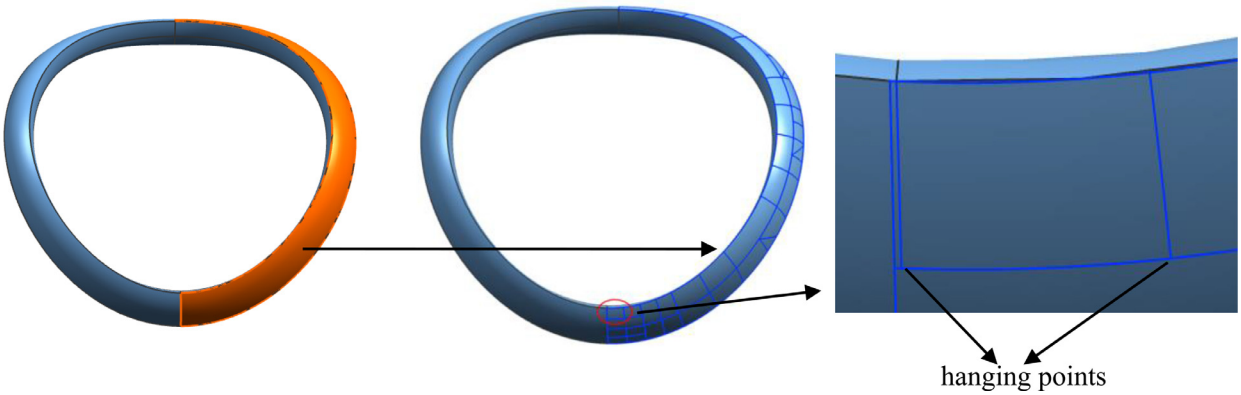


**Fig. 4.** Face discretized by discontinuous grids.

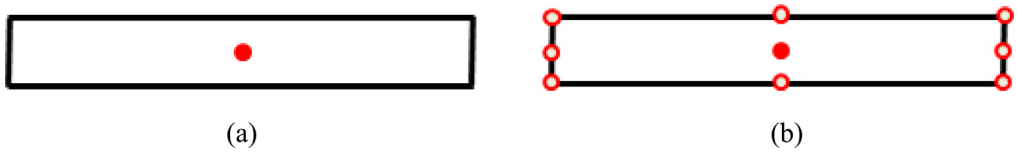


**Fig. 5.** Constant elements: (a) Conventional discontinuous element in BFM, (b) Dual interpolation element in DiBFM.

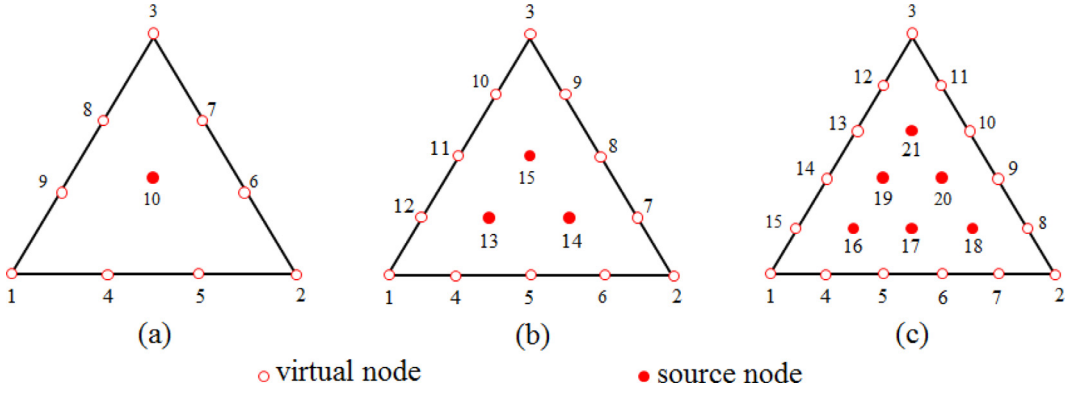


**Fig. 6.** Dual interpolation elements for triangle: (a) TS1, (b) TS3, and (c) TS6.

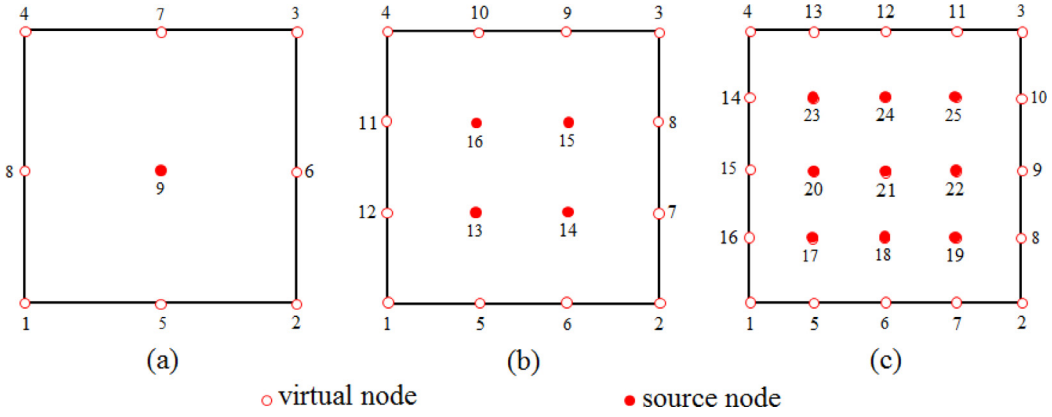


**Fig. 7.** Dual interpolation elements for quadrilateral: (a) QS1, (b) QS4, and (c) QS9.

tual nodes and the source nodes are considered, it amounts to a standard continuous element. In this manner, the continuous and discontinuous element schemes can be unified by the dual interpolation element.

In Fig. 6, the elements are identified with the notation TS1, TS3 and TS6 and in Fig. 7 the elements are identified with the notation QS1, QS4 and QS9, where T denotes the triangular element, and Q denotes the quadrilateral element. The Si means that there are i source nodes in the continuous element. This notation is based on the fact that the degrees of freedom associated with the virtual nodes are eliminated, so that they do not appear in the system equations in DiBFM.

Compared with the interpolation function order of the conventional discontinuous elements which use the source nodes only, the addition of

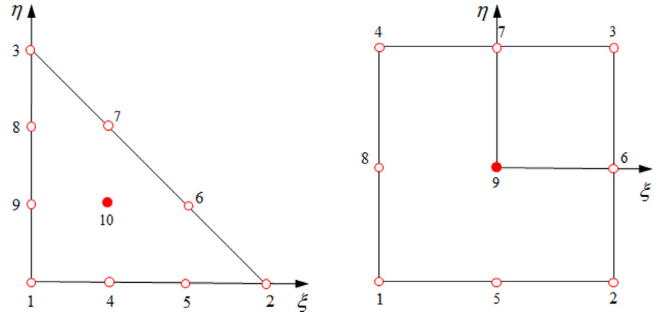


**Fig. 8.** Local parametric coordinate in element: TS1 and QS1.

virtual nodes introduced in dual interpolation elements signifies that the interpolation order in the dual interpolation elements is increased. For 2D problems, the interpolation order in the dual interpolation elements increases with two orders, which results in a significant improvement in numerical simulation [1]. It is expected that this feature can be extended to 3D problems.

### 3.2. The first-layer interpolation

The first-layer interpolation is similar to the interpolation in a conventional continuous boundary element, i.e. both source nodes and virtual nodes are taken into account in a dual interpolation element. Thus, for an arbitrary quantity$\phi$, the interpolation form is:

$$\varphi(\xi,\eta)=\sum_{\alpha=1}^{n_s}N_\alpha^s(\xi,\eta)\varphi(Q_\alpha^s)+\sum_{\beta=1}^{n_v}N_\beta^v(\xi,\eta)\varphi(Q_\beta^v) \tag{1}$$

where$N_\alpha^s(\xi,\eta)$and $N_\beta^v(\xi,\eta)$denote the shape functions of the source node $\alpha$ and virtual node $\beta$,$\varphi(Q_\alpha^s)$and $\varphi(Q_\beta^v)$are the nodal values, $n_s$ and $n_v$ denote the numbers of source nodes and virtual nodes in total in the dual interpolation element, respectively. Normalized coordinate$\xi,\ \eta\in[-1,1]$. In DiBFM, the virtual nodal value $\varphi(Q_\beta^v)$depends on the nodal values of the source nodes which are to be determined by the second-layer interpolation.

It is noted that the shape functions $N_\alpha^s(\xi,\eta)$and $N_\beta^v(\xi,\eta)$in Eq. (1) are the Lagrange polynomials used in a conventional element with a number of nodes $(n_s+n_v)$. The derivation of the shape functions of the above elements can be referred to the work [21]. Here, only the shape functions for element TS1 and QS1 shown in Fig. 8 are given as

$$\begin{cases}N_1=N_1^v(\xi,\eta)=0.5(3\xi-1)(3\xi-2)\xi & N_6=N_6^v(\xi,\eta)=4.5\eta(1-\xi-\eta)(3\eta-1)\\ N_2=N_2^v(\xi,\eta)=0.5(3\eta-1)(3\eta-2)\eta & N_7=N_7^v(\xi,\eta)=4.5\eta(1-\xi-\eta)(2-3\xi-3\eta)\\ N_3=N_3^v(\xi,\eta)=0.5(2-3\xi-3\eta)(1-3\xi-3\eta)(1-\xi-\eta) & N_8=N_8^v(\xi,\eta)=4.5\xi(1-\xi-\eta)(2-3\xi-3\eta)\\ N_4=N_4^v(\xi,\eta)=4.5\xi\eta(3\xi-1) & N_9=N_9^v(\xi,\eta)=4.5\xi(1-\xi-\eta)(3\xi-1)\\ N_5=N_5^v(\xi,\eta)=4.5\xi\eta(3\eta-1) & N_{10}=N_1^s(\xi,\eta)=27\xi\eta(1-\xi-\eta)\end{cases} \tag{2}$$

and

$$\begin{cases}N_1=N_1^v(\xi,\eta)=0.25\xi\eta(\xi-1)(\eta-1) & N_5=N_5^v(\xi,\eta)=0.5\eta\left(1-\xi^2\right)(\eta-1)\\ N_2=N_2^v(\xi,\eta)=0.25\xi\eta(\xi+1)(\eta-1) & N_6=N_6^v(\xi,\eta)=0.5\xi(\xi+1)\left(1-\eta^2\right)\\ N_3=N_3^v(\xi,\eta)=0.25\xi\eta(\xi+1)(\eta+1) & N_7=N_7^v(\xi,\eta)=0.5\eta\left(1-\xi^2\right)(\eta+1)\\ N_4=N_4^v(\xi,\eta)=0.25\xi\eta(\xi-1)(\eta+1) & N_8=N_8^v(\xi,\eta)=0.5\xi(\xi-1)\left(1-\eta^2\right)\\ N_9=N_1^s(\xi,\eta)=\left(1-\xi^2\right)\left(1-\eta^2\right)\end{cases} \tag{3}$$

respectively.

### 3.3. The second-layer interpolation

Same as in 2D problems [1,2], the second-layer interpolation is just utilized to construct the relationships between source and virtual nodes, rather than evaluating the shape function of each Gauss point in the boundary integration. These relationships are employed to condense the degrees of freedom associated with virtual nodes. In this paper, the second-layer interpolation is constructed by the moving least square (MLS) method which is suitable to approximate both continuous and discontinuous fields particularly to treat the problems with sharp edges and corners.

#### 3.3.1. The moving least square approximation

The approximation with MLS approximation is applied to construct the second-layer interpolation. And it is independently performed on each boundary surface. The virtual nodal value is approximated by:

$$\varphi(Q_\beta^v)=\sum_{m=1}^{M}\psi_m^{vs}(u_\beta^v,v_\beta^v)\varphi(Q_m^s) \tag{4}$$

where $M$ denotes the number of source nodes $Q_m^s$covered in the influence domain of virtual node $Q_\beta^v$,$\psi_m^{vs}(u_\beta^v,v_\beta^v)$denotes the shape function of the second-layer interpolation corresponding to source node $Q_m^s$,$u_\beta^v$and $v_\beta^v$are the parametric coordinate of the virtual node $Q_\beta^v$. The parametric coordinate is employed to locate a point on a boundary surface. For the shape functions of MLS approximation corresponding to all source nodes, which can be expressed as

$$\boldsymbol{\psi}=\{\psi_1^{vs},\psi_2^{vs},\ldots,\psi_j^{vs},\ldots,\psi_M^{vs}\}=\boldsymbol{p}^T(u,v)\boldsymbol{A}^{-1}(u,v)\boldsymbol{B}(u,v) \tag{5}$$

with matrices $p^T(u,v)$,$A(u,v)$ and $B(u,v)$ defined by

$$\boldsymbol{p}^T=\left[1,u,v,u^2,uv,v^2\right]$$

$$\boldsymbol{A}(u,v)=\sum_{m=1}^{M}w_m\boldsymbol{p}(u_m,v_m)\boldsymbol{p}^T(u_m,v_m)$$

$$\boldsymbol{B}(u,v)=\left[w_1\boldsymbol{p}(u_1,v_1),w_2\boldsymbol{p}(u_2,v_2),\ldots w_M\boldsymbol{p}(u_M,v_M)\right]$$

where $w_m$ is the weight function corresponding to a node$(u_m,v_m)$. The $\psi_m^{vs}(u_\beta^v,v_\beta^v)$is usually called the shape function of the MLS approximation corresponding to the source node$Q_m^s(u_m,v_m)$. More details of the MLS approximation are available in [22].

The influence domain of virtual node in this paper is the neighboring three-layer elements around the virtual node. Since the MLS approximation is independently performed on each boundary surface, the three-layer elements are only searched on the boundary surface where the virtual point is located, and not on other boundary surfaces.

#### 3.3.2. Approximation of continuous and discontinuous fields

To illustrate the dual interpolation method can approximate continuous and discontinuous fields, the cube discretized by the dual interpolation elements will be used as an example (see Fig. 9).

As shown in Fig. 9, one virtual node is placed at a point where adjacent elements are smoothly connected, so that the four elements share the same virtual node. However, more than one virtual nodes are placed at geometric corner, geometric edge or point where the boundary conditions are not continuous, and the elements on same boundary surface share one virtual node.

For a point on smooth boundary, only a single virtual node is placed (see the point **p** in Fig. 9). The source points covered by the influence domain of the virtual node $v_0$, are shown in Fig. 10(a). For 3D elasticity problems, the independent physical variables on the boundary are displacements $u_i$ and tractions $t_i$ $(i=1,2,3)$. Based on the MLS approximation in Eq. (4), the second-layer interpolations of these two variables are expressed as:

$$u_i(Q_{v_0}^v)=\sum_{m=1}^{M}\psi_m^{vs}(u_{v_0}^v,v_{v_0}^v)u_i(Q_m^s) \tag{6}$$

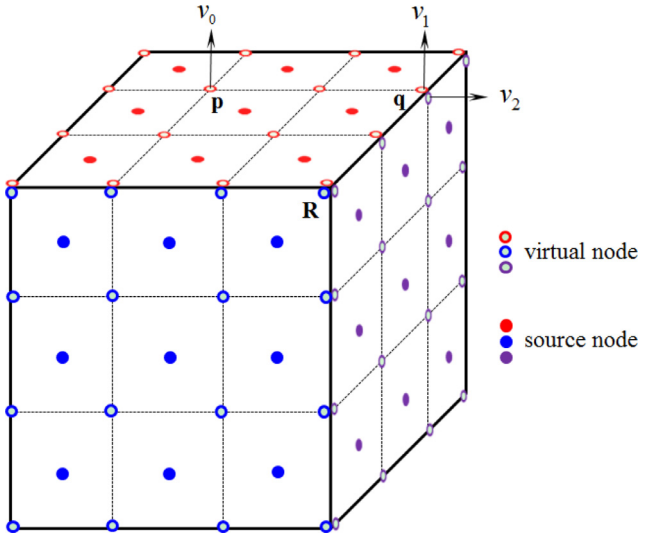


**Fig. 9.** Approximation of continuous and discontinuous fields.

$$t_i(Q^v_{v_0}) = \sum_{m=1}^{M} \psi_m^{vs}(u^v_{v_0}, v^v_{v_0}) t_i(Q^s_m) \tag{7}$$

where the number (M) of source points, which is covered by influence domain of the virtual node $v_0$, is nine(see Fig. 10(a)).

For a corner point, more than one virtual nodes are placed. The two virtual nodes, $v_0$ and $v_1$, are collocated at the point **q** (see Fig. 9). Since these two virtual nodes are on different boundary surfaces, the influence domains of these two virtual nodes are naturally different (see Fig. 10(b) and (c)). To model the discontinuous traction field at the virtual node $v_1$ and $v_2$, the tractions $t_i(Q^v_{v_1})$and $t_i(Q^v_{v_2})(i = 1, 2, 3)$ are still calculated by Eq. (7). To ensure that the displacement field at the virtual node $v_1$ and $v_2$ is continuous, the displacement $u_i(Q^v_{v_1})$and $u_i(Q^v_{v_2})$are calculated by:

$$u_i(Q^v_{v_k}) = \frac{1}{K} \sum_{k=1}^{K} \sum_{m=1}^{M} \psi_m^{vs}(u^v_{v_k}, v^v_{v_k}) u_i(Q^s_m) \tag{8}$$

Where *K*denotes the number of the virtual nodes at the corner point. At the corner point **q**, $K = 2$.

From Eqs. (6)–(8), the dual interpolation method has the ability to approximate the continuous and discontinuous fields via manipulating the influence domain of virtual nodes in the second-layer interpolation. The second-layer interpolation is further described in the flow diagram shown in Fig. 11.

## 4. DiBFM for elasticity problem

### 4.1. Boundary integral equation for 3D elasticity

Consider an elasticity body occupying domain $\Omega \subset \mathbf{R}^3$ with boundary Γ. The boundary integral equation (BIE) [23] of elasticity without body

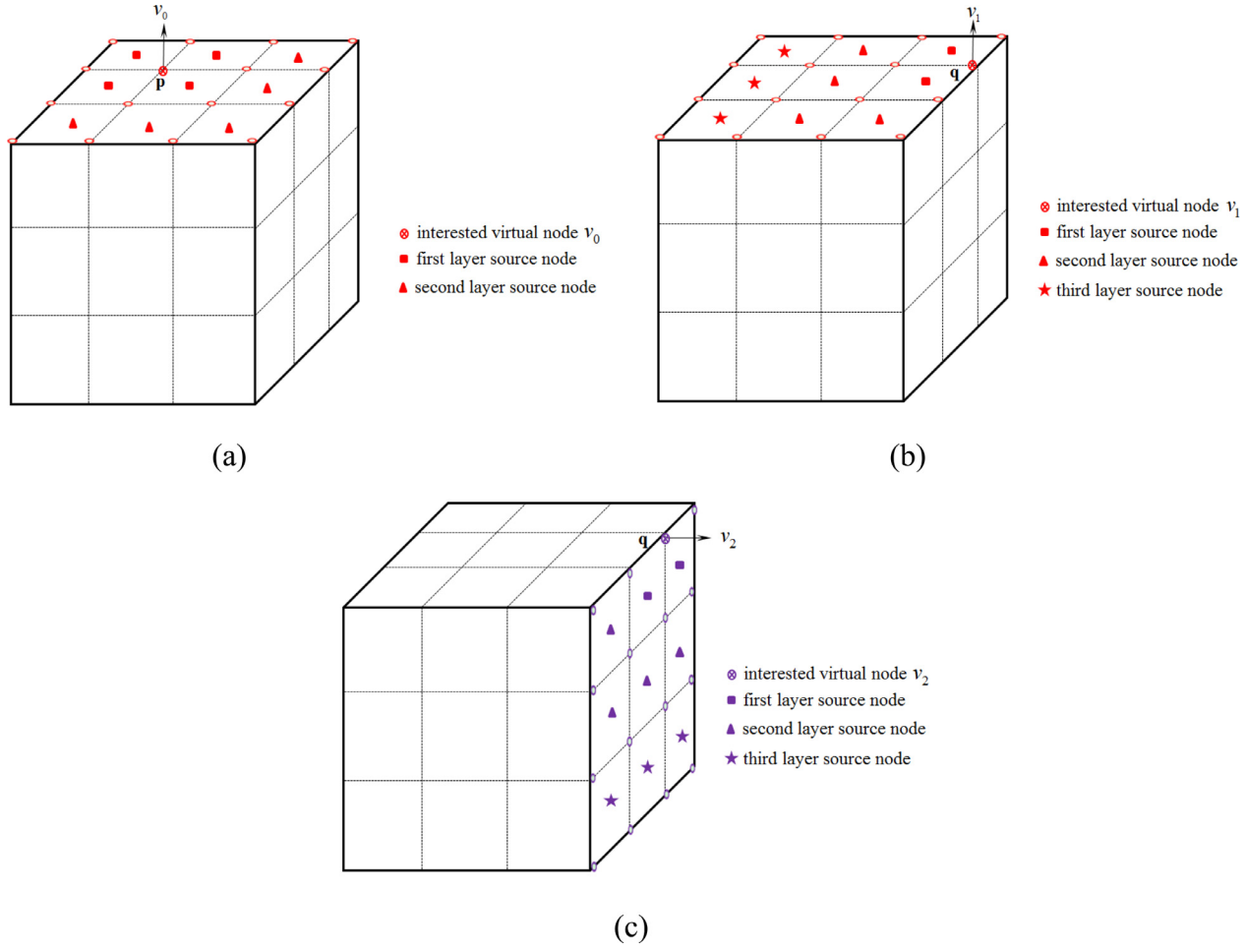


**Fig. 10.** Influence domain of the virtual nodes: (a) virtual node $v_0$, (b) virtual node $v_1$, (c) virtual node $v_2$.

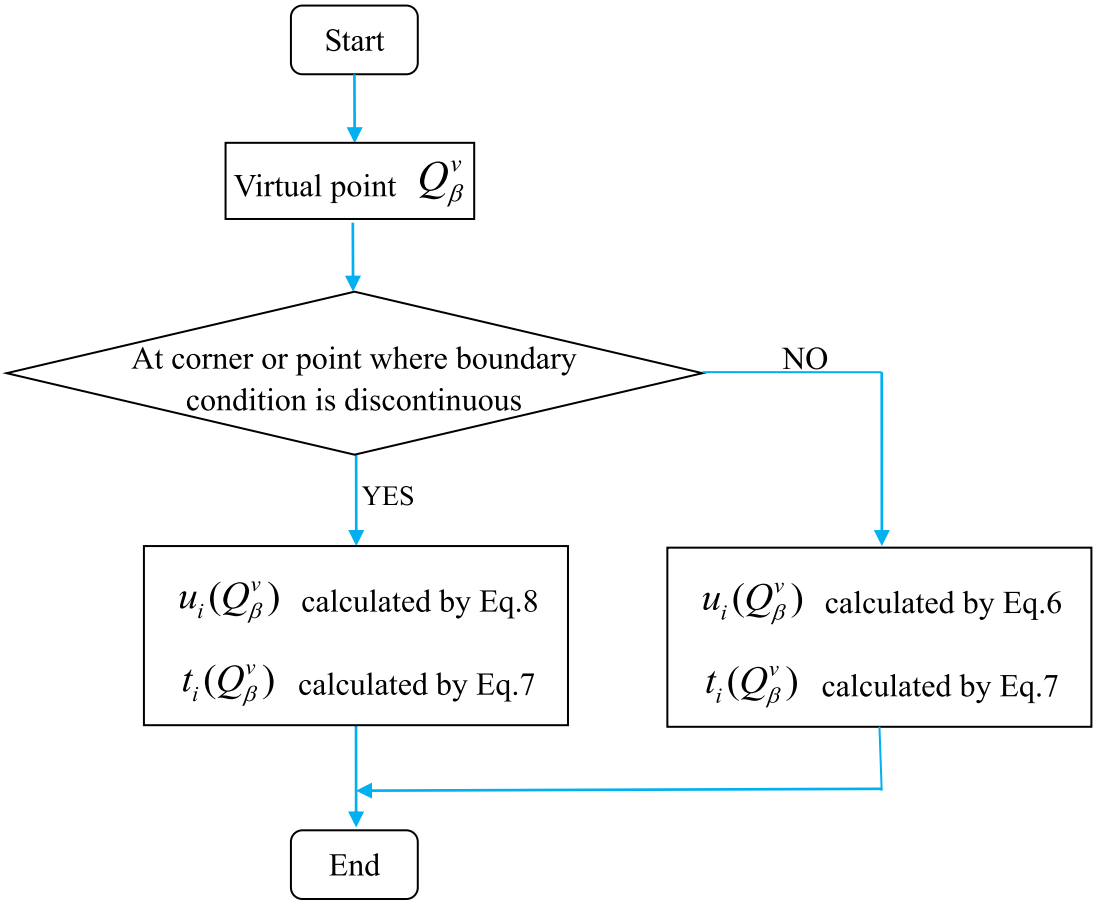


**Fig. 11.** Flow diagram of the second-layer interpolation.

force can be written as:

$$c_{ij}(P)u_j(P) = \int_\Gamma U_{ij}(P,Q)t_j(Q)d\Gamma(Q) - \int_\Gamma T_{ij}(P,Q)u_j(Q)d\Gamma(Q), \qquad P,Q \in \Gamma \tag{9}$$

where $u_j$ is displacement, $t_j$is traction, $i,j$ = (1, 2, 3) and $c_{ij}(P)$ is coefficient which depends on the boundary configuration. The $U_{ij}(P,Q)$ and $T_{ij}(P,Q)$ are fundamental solutions of displacement and traction as follow:

$$U_{ij}(P,Q) = \frac{1}{16\pi G(1-\nu)r}\left[(3-4\nu)\delta_{ij} + r_{,i}r_{,j}\right] \tag{10}$$

$$T_{ij}(P,Q) = \frac{1}{8\pi(1-\nu)r^2}\left\{\frac{\partial r}{\partial n}\left[(1-2\nu)\delta_{ij} + 3r_{,i}r_{,j}\right] + (1-2\nu)(n_j r_{,i} - n_i r_{,j})\right\} \tag{11}$$

where $r$ denotes the distance between the source node $P$ and the field point $Q$, and $n(n_1,n_2,n_3)$ is the unit outward normal at the point $Q$,$\nu$ denotes the Poisson's ratio and $G$ is the shear modulus.

### 4.2. Discretization of the BIE for 3D elasticity

In the DiBFM, the BIE is discretized by dual interpolation elements, and only the source nodes $P_k$ ($k$ = 1,2,…,NS) are collocated. The NS is the total number of source nodes in all elements. After discretizing, the BIE in Eq. (9) yields:

$$\sum_{e=1}^{ne}\left[\sum_{\alpha=1}^{n_s} h_{ij}^{ss}(P_k)u_j(Q_{e(a)}^s) + \sum_{\beta=1}^{n_v} h_{ij}^{sv}(P_k)u_j(Q_{e(\beta)}^v)\right] = \sum_{e=1}^{ne}\left[\sum_{\alpha=1}^{n_s} g_{ij}^{ss}(P_k)t_j(Q_{e(a)}^s) + \sum_{\beta=1}^{n_v} g_{ij}^{sv}(P_k)t_j(Q_{e(\beta)}^v)\right] \tag{12}$$

in which

$$h_{ij}^{ss}(P_k) = \int_{\Gamma_e} T_{ij}(P_k,Q)N_{e(\alpha)}^s(Q)d\Gamma(Q) + \frac{1}{2}\delta_{ij}\delta_{e(\alpha)}^k$$

$$h_{ij}^{sv}(P_k) = \int_{\Gamma_e} T_{ij}(P_k,Q)N_{e(\beta)}^v(Q)d\Gamma(Q)$$

$$g_{ij}^{ss}(P_k) = \int_{\Gamma_e} U_{ij}(P_k,Q)N_{e(\alpha)}^s(Q)d\Gamma(Q)$$

$$g_{ij}^{sv}(P_k) = \int_{\Gamma_e} U_{ij}(P_k,Q)N_{e(\beta)}^v(Q)d\Gamma(Q)$$

and

$$\delta_{e(\alpha)}^k = \begin{cases} 1, \text{if source node } P_k \text{ is the } \alpha\text{th source node in the } e\text{th element} \\ 0, \end{cases}$$

where $\Gamma_e$ denotes the boundary of the $e$th element, $N_{e(\alpha)}^s$,$t_j(Q_{e(a)}^s)$and $u_j(Q_{e(a)}^s)$indicate the shape function, nodal values of the traction and displacement of the $\alpha$th source node in the $e$th element. $N_{e(\beta)}^v$,$t_j(Q_{e(\beta)}^v)$and $u_j(Q_{e(\beta)}^v)$are the shape function, nodal values of the traction and displacement of the $\beta$th virtual node in the $e$th element. The definitions of $n_s$and $n_v$ are given in Section 3.2. Eq. (12) can be arranged in a matrix form as:

$$\sum_{j=1}^{3}\left(\begin{bmatrix}\mathbf{H}_{1j}^{ss}\\ \mathbf{H}_{2j}^{ss}\\ \mathbf{H}_{3j}^{ss}\end{bmatrix}\left\{\mathbf{u}_j^s\right\} + \begin{bmatrix}\mathbf{H}_{1j}^{sv}\\ \mathbf{H}_{2j}^{sv}\\ \mathbf{H}_{3j}^{sv}\end{bmatrix}\left\{\mathbf{u}_j^v\right\}\right) = \sum_{j=1}^{3}\left(\begin{bmatrix}\mathbf{G}_{1j}^{ss}\\ \mathbf{G}_{2j}^{ss}\\ \mathbf{G}_{3j}^{ss}\end{bmatrix}\left\{\mathbf{t}_j^s\right\} + \begin{bmatrix}\mathbf{G}_{1j}^{sv}\\ \mathbf{G}_{2j}^{sv}\\ \mathbf{G}_{3j}^{sv}\end{bmatrix}\left\{\mathbf{t}_j^v\right\}\right) \tag{13}$$

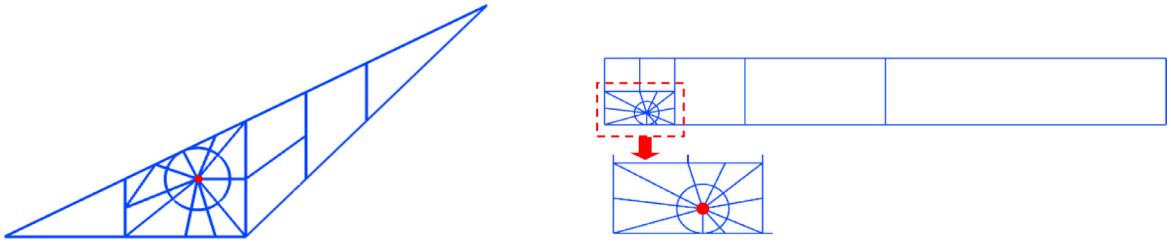

(a) Obtuse triangle element. (b) Slender quadrilateral element.

**Fig. 12.** The irregular elements subdivision results of the BTSM.

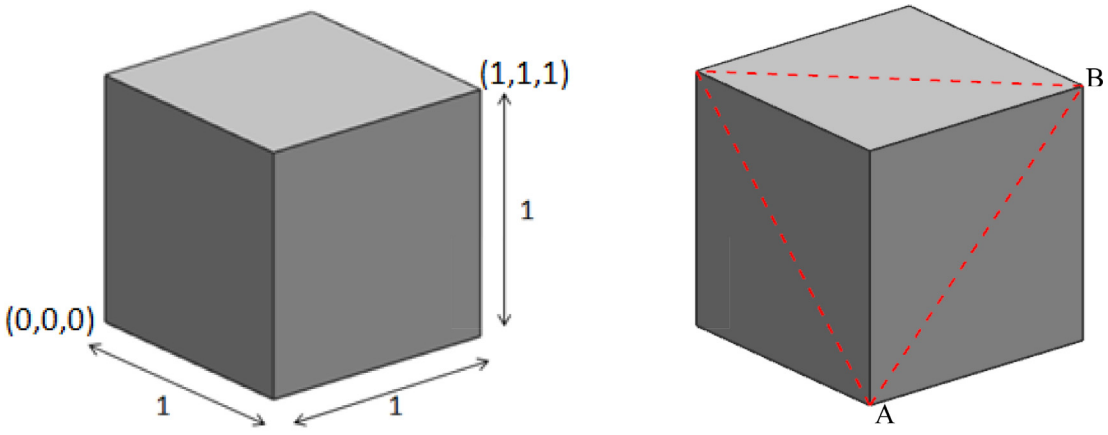


(a) Geometric model (b) The distribution of the sample points

**Fig. 13.** The analytical field problem on a cube.

**Table 1**
Numerical evaluation of weakly singular integral for irregular elements.

| Element type | Gaussian points number | | Relative error | |
|---|---|---|---|---|
| | CSM | BTSM | CSM | BTSM |
| Obtuse triangle element (Fig. 12(a)) | 115 | 115 | 5.2171e-002 | 1.1403e-003 |
| | 151 | 151 | 2.4437e-002 | 1.7927e-004 |
| | 280 | 280 | 3.1383e-003 | 1.1393e-005 |
| | 450 | 450 | 1.4306e-003 | 6.5192e-007 |
| Slender quadrilateral element (Fig. 12(b)) | 122 | 122 | 3.7711e-002 | 1.7351e-003 |
| | 199 | 199 | 2.3095e-002 | 2.1645e-005 |
| | 347 | 347 | 1.2658e-002 | 3.5789e-006 |
| | 527 | 527 | 5.4994e-003 | 9.7340e-007 |

where $\mathbf{u}_j^s$and $\mathbf{t}_j^s$denote the vectors of displacement and traction for all source nodes, $\mathbf{u}_j^v$and $\mathbf{t}_j^v$are displacement and traction vectors for all virtual nodes. $\mathbf{H}_{ij}^{ss}$,$\mathbf{G}_{ij}^{ss}$,$\mathbf{H}_{ij}^{sv}$and $\mathbf{G}_{ij}^{sv}$are the coefficient matrices corresponding to vectors $\mathbf{u}_j^s$,$\mathbf{t}_j^s$,$\mathbf{u}_j^v$and $\mathbf{t}_j^v$, respectively. Considering the boundary conditions, we can rewrite Eq. (13)as:

$$\sum_{j=1}^{3}\left(\begin{bmatrix}\mathbf{H}_{1d_j}^{ss} & \mathbf{H}_{1n_j}^{ss}\\ \mathbf{H}_{2d_j}^{ss} & \mathbf{H}_{2n_j}^{ss}\\ \mathbf{H}_{3d_j}^{ss} & \mathbf{H}_{3n_j}^{ss}\end{bmatrix}\begin{Bmatrix}\bar{\mathbf{u}}_{d_j}^s\\ \mathbf{u}_{n_j}^s\end{Bmatrix}+\begin{bmatrix}\mathbf{H}_{1d_j}^{sv} & \mathbf{H}_{1n_j}^{sv}\\ \mathbf{H}_{2d_j}^{sv} & \mathbf{H}_{2n_j}^{sv}\\ \mathbf{H}_{3d_j}^{sv} & \mathbf{H}_{3n_j}^{sv}\end{bmatrix}\begin{Bmatrix}\bar{\mathbf{u}}_{d_j}^v\\ \mathbf{u}_{n_j}^v\end{Bmatrix}\right)$$
$$=\sum_{j=1}^{3}\left(\begin{bmatrix}\mathbf{G}_{1d_j}^{ss} & \mathbf{G}_{1n_j}^{ss}\\ \mathbf{G}_{2d_j}^{ss} & \mathbf{G}_{2n_j}^{ss}\\ \mathbf{G}_{3d_j}^{ss} & \mathbf{G}_{3n_j}^{ss}\end{bmatrix}\begin{Bmatrix}\mathbf{t}_{d_j}^s\\ \bar{\mathbf{t}}_{n_j}^s\end{Bmatrix}+\begin{bmatrix}\mathbf{G}_{1d_j}^{sv} & \mathbf{G}_{1n_j}^{sv}\\ \mathbf{G}_{2d_j}^{sv} & \mathbf{G}_{2n_j}^{sv}\\ \mathbf{G}_{3d_j}^{sv} & \mathbf{G}_{3n_j}^{sv}\end{bmatrix}\begin{Bmatrix}\mathbf{t}_{d_j}^v\\ \bar{\mathbf{t}}_{n_j}^v\end{Bmatrix}\right) \tag{14}$$

where the subscripts $d_j$ and $n_j$ indicate the Dirichlet (displacement) and Neumann (traction) boundary conditions, $\bar{\mathbf{u}}_{d_j}^s$,$\bar{\mathbf{u}}_{d_j}^v$,$\bar{\mathbf{t}}_{n_j}^s$and $\bar{\mathbf{t}}_{n_j}^v$are vectors of the displacement and the traction of the source node and the virtual node specified in the direction $j$, respectively.

### 4.3. Reduction of the degrees of freedom

As presented in the Section 3.1, the source points $P$ in BIEs in Eq. (9) are collocated at source nodes. Thus, the number of linear algebraic equations is less than unknown number of the nodal value in Eq. (14). In order to make the equations be solvable, additional constraint equations are needed. The additional constraints are provided by the second-layer interpolation as:

$$\left\{\mathbf{u}_{n_j}^v\right\}=\mathbf{\Psi}_{n_jn_j}^{vs}\left\{\mathbf{u}_{n_j}^s\right\},j=(1,2,3) \tag{15}$$

$$\left\{\mathbf{t}_{d_j}^v\right\}=\mathbf{\Theta}_{d_jd_j}^{vs}\left\{\mathbf{t}_{d_j}^s\right\},j=(1,2,3) \tag{16}$$

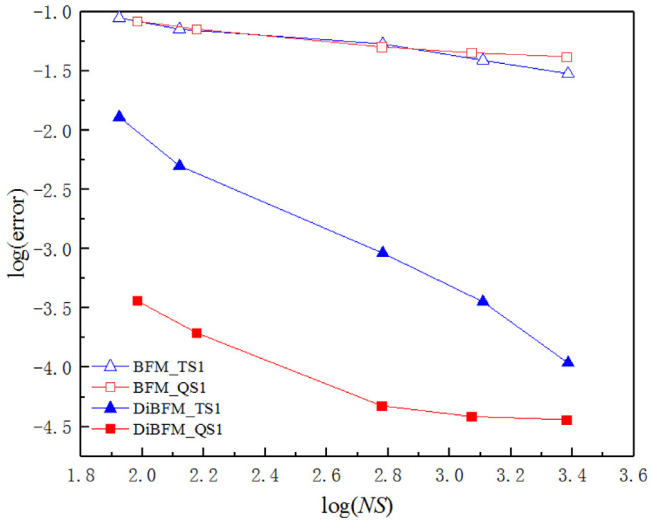


**Fig. 14.** Comparison of convergence behavior between the BFM and the DiBFM.

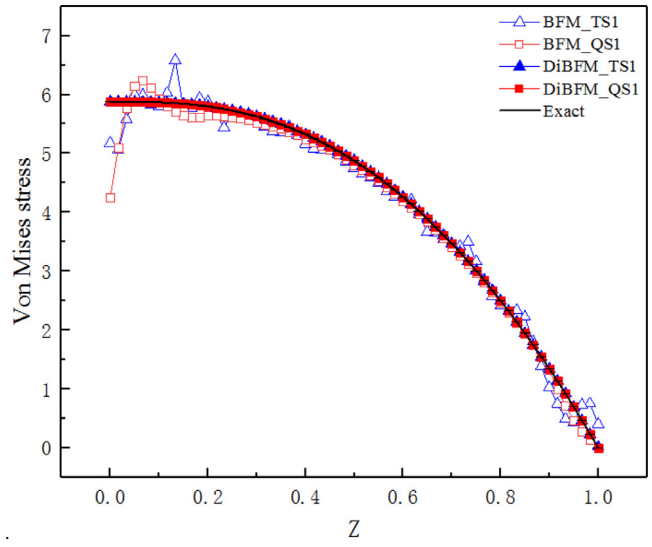


**Fig. 15.** Comparison of accuracy for Von Misses stress along the line AB.

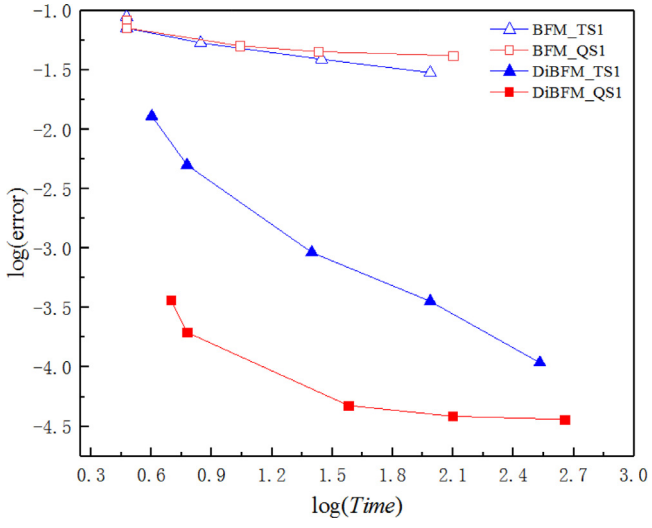


**Fig. 16.** Comparison of computational efficiency between the BFM and the DiBFM.

where $\boldsymbol{\Psi}^{vs}_{n_j n_j}$ and $\boldsymbol{\Theta}^{vs}_{d_j d_j}$ denote the second-layer interpolation shape function matrices of the displacement and traction, respectively (see Section 3).

Substituting Eqs. (15) and (16) into Eq. (14) results

$$\sum_{j=1}^{3}\left(\begin{bmatrix}\mathbf{H}^{ss}_{1d_j} & \bar{\mathbf{H}}^{ss}_{1n_j}\\ \mathbf{H}^{ss}_{2d_j} & \bar{\mathbf{H}}^{ss}_{2n_j}\\ \mathbf{H}^{ss}_{3d_j} & \bar{\mathbf{H}}^{ss}_{3n_j}\end{bmatrix}\begin{Bmatrix}\bar{\mathbf{u}}^{s}_{d_j}\\ \mathbf{u}^{s}_{n_j}\end{Bmatrix}+\begin{bmatrix}\mathbf{H}^{sv}_{1d_1}\\ \mathbf{H}^{sv}_{2d_1}\\ \mathbf{H}^{sv}_{3d_1}\end{bmatrix}\begin{Bmatrix}\bar{\mathbf{u}}^{v}_{d_j}\end{Bmatrix}\right)$$
$$=\sum_{j=1}^{3}\left(\begin{bmatrix}\bar{\mathbf{G}}^{ss}_{1d_j} & \mathbf{G}^{ss}_{1n_j}\\ \bar{\mathbf{G}}^{ss}_{2d_j} & \mathbf{G}^{ss}_{2n_j}\\ \bar{\mathbf{G}}^{ss}_{3d_j} & \mathbf{G}^{ss}_{3n_j}\end{bmatrix}\begin{Bmatrix}\mathbf{t}^{s}_{d_j}\\ \bar{\mathbf{t}}^{s}_{n_j}\end{Bmatrix}+\begin{bmatrix}\mathbf{G}^{sv}_{1n_1}\\ \mathbf{G}^{sv}_{2n_1}\\ \mathbf{G}^{sv}_{3n_1}\end{bmatrix}\begin{Bmatrix}\bar{\mathbf{t}}^{v}_{n_j}\end{Bmatrix}\right) \tag{17}$$

in which

$$\begin{bmatrix}\bar{\mathbf{H}}^{ss}_{1n_j}\\ \bar{\mathbf{H}}^{ss}_{2n_j}\\ \bar{\mathbf{H}}^{ss}_{3n_j}\end{bmatrix}=\begin{bmatrix}\mathbf{H}^{ss}_{1n_j}\\ \mathbf{H}^{ss}_{2n_j}\\ \mathbf{H}^{ss}_{3n_j}\end{bmatrix}+\begin{bmatrix}\mathbf{H}^{sv}_{1n_j}\\ \mathbf{H}^{sv}_{2n_j}\\ \mathbf{H}^{sv}_{3n_j}\end{bmatrix}\boldsymbol{\Psi}^{cs}_{n_j n_j}$$

$$\begin{bmatrix}\bar{\mathbf{G}}^{ss}_{1d_j}\\ \bar{\mathbf{G}}^{ss}_{2d_j}\\ \bar{\mathbf{G}}^{ss}_{3d_j}\end{bmatrix}=\begin{bmatrix}\mathbf{G}^{ss}_{1d_j}\\ \mathbf{G}^{ss}_{2d_j}\\ \mathbf{G}^{ss}_{3d_j}\end{bmatrix}+\begin{bmatrix}\mathbf{G}^{sv}_{1d_j}\\ \mathbf{G}^{sv}_{2d_j}\\ \mathbf{G}^{sv}_{3d_j}\end{bmatrix}\boldsymbol{\Theta}^{cs}_{d_j d_j}$$

### 4.4. Numerical solution for 3D elasticity

Imposing the boundary conditions at each source and virtual node and exchanging the columns of matrices in Eq. (17), the final system equations can be rewritten as:

$$\mathbf{Ax}=\mathbf{b} \tag{18}$$

in which

$$\mathbf{A}=\begin{bmatrix}-\bar{\mathbf{G}}^{ss}_{1d_1} & \bar{\mathbf{H}}^{ss}_{1n_1} & -\bar{\mathbf{G}}^{ss}_{1d_2} & \bar{\mathbf{H}}^{ss}_{1n_2} & -\bar{\mathbf{G}}^{ss}_{1d_3} & \bar{\mathbf{H}}^{ss}_{1n_3}\\ -\bar{\mathbf{G}}^{ss}_{2d_1} & \bar{\mathbf{H}}^{ss}_{2n_1} & -\bar{\mathbf{G}}^{ss}_{2d_2} & \bar{\mathbf{H}}^{ss}_{2n_2} & -\bar{\mathbf{G}}^{ss}_{2d_3} & \bar{\mathbf{H}}^{ss}_{2n_3}\\ -\bar{\mathbf{G}}^{ss}_{3d_1} & \bar{\mathbf{H}}^{ss}_{3n_1} & -\bar{\mathbf{G}}^{ss}_{3d_2} & \bar{\mathbf{H}}^{ss}_{3n_2} & -\bar{\mathbf{G}}^{ss}_{3d_3} & \bar{\mathbf{H}}^{ss}_{3n_3}\end{bmatrix}$$

$$\mathbf{x}=\begin{Bmatrix}\mathbf{t}^{s}_{d_1} & \mathbf{u}^{s}_{n_1} & \mathbf{t}^{s}_{d_2} & \mathbf{u}^{s}_{n_2} & \mathbf{t}^{s}_{d_3} & \mathbf{u}^{s}_{n_3}\end{Bmatrix}^{\mathrm{T}}$$

$$\mathbf{b}=\sum_{j=1}^{3}\left(\begin{bmatrix}-\mathbf{H}^{ss}_{1d_j} & \mathbf{G}^{ss}_{1n_j}\\ -\mathbf{H}^{ss}_{2d_j} & \mathbf{G}^{ss}_{2n_j}\\ -\mathbf{H}^{ss}_{3d_j} & \mathbf{G}^{ss}_{3n_j}\end{bmatrix}\begin{Bmatrix}\bar{\mathbf{u}}^{s}_{d_j}\\ \bar{\mathbf{t}}^{s}_{n_j}\end{Bmatrix}+\begin{bmatrix}-\mathbf{H}^{sv}_{1d_j} & \mathbf{G}^{sv}_{1n_j}\\ -\mathbf{H}^{sv}_{2d_j} & \mathbf{G}^{sv}_{2n_j}\\ -\mathbf{H}^{sv}_{3d_j} & \mathbf{G}^{sv}_{3n_j}\end{bmatrix}\begin{Bmatrix}\bar{\mathbf{u}}^{v}_{d_j}\\ \bar{\mathbf{t}}^{v}_{n_j}\end{Bmatrix}\right)$$

For 3D elasticity problems, the size of matrix **A** is 3NS, **x** is unknown at the source node, and **b** is known with boundary conditions.

In this paper, the Gaussian elimination method [24] is used to obtain solutions in Eq. (18). By using the second-layer interpolation in Eqs. (15) and (16), all nodal values at virtual nodes can be determined.

Due to the unknown vector of the final system equations involving the source node only, the size of the final system equations in the DiBFM is the same as that in the conventional BEM using source nodes alone seeing from Eq. (18). As a result, the efficiency in DiBFM remains unchanged.

### 4.5. The binary-tree subdivision method for evaluation of singular integrals

In order to evaluate the singular integrals in Eq. (12), the binary-tree subdivision method (BTSM) [20] is employed. Even if the shape of an element is very irregular, the BTSM can evaluate singular integrals accurately for cases of arbitrary location of the source point. This is because the resulting subdivision sub-elements distribution is dense close to the source point and sparse far from the source point, while the source point is isolated with a circular cavity that is subdivided using regular triangular elements converging on the source point. In the BTSM, an element is

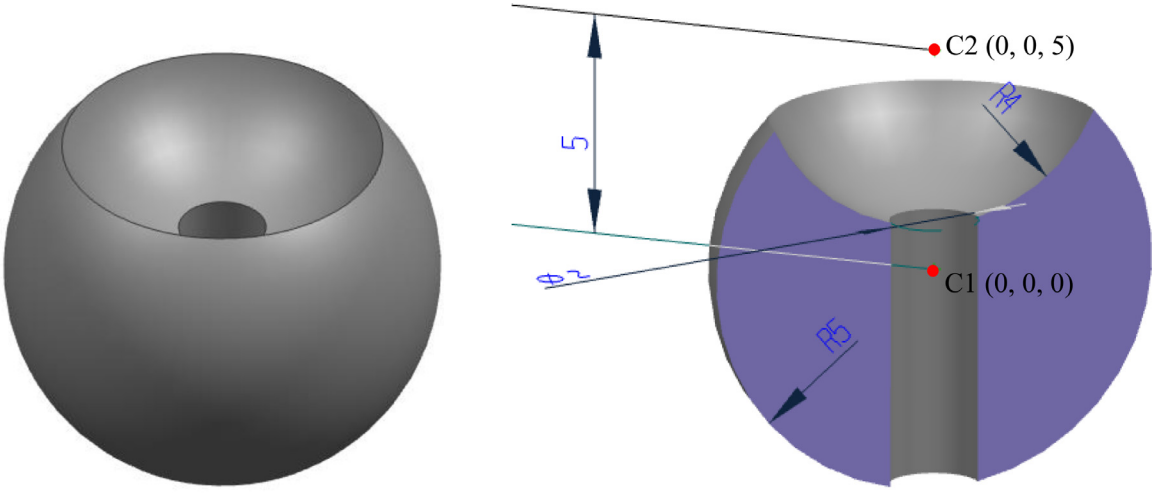


(a) A trimmed sphere.

(b) Main dimension and Sectional view.

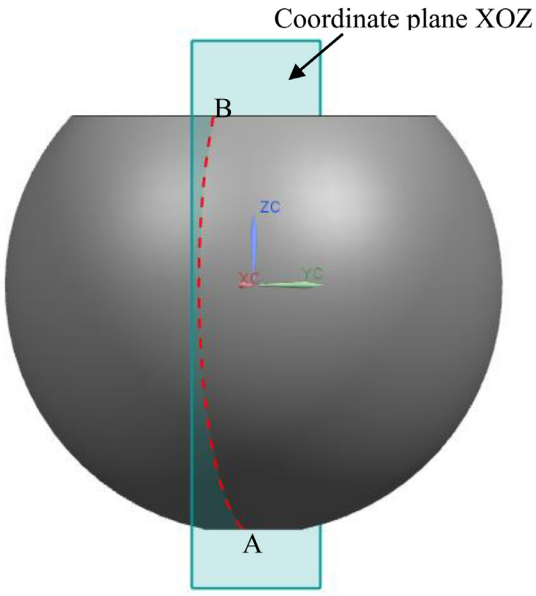


(c) The distribution of the sample points.

**Fig. 17.** The analytical field problem on a trimmed sphere.

split into two sub-elements at each step, and continues the splitting process recursively until meeting a given terminating criterion. Fig. 12 and Table 1 show two examples of irregular elements. Exploiting BTSM can guarantee that the computational error comes from integration will be restricted to a very low level, and hence, significantly improve the stability for elasticity computation. For more details, please refer to [20]. where the CSM denotes the Conventional Subdivision Method whose sub-elements are obtained by simply connecting the source point with each vertex of the element.

## 5. Numerical examples

In this section, four examples are presented. The first two examples are used to demonstrate the accuracy and efficiency of the DiBFM for solving 3D elastic problems. The other two examples demonstrate further the high accuracy of the proposed method for realistic engineering problems. All computations were executed on a desktop computer with an Intel® Core™ i7–3770 K, 3.5 GHz processor and 32 GB of RAM.

The accuracy and efficiency of the DiBFM are demonstrated by comparison with the BFM. The DiBFM_QS1 denotes the DiBFM with the elements QS1, and the DiBFM_TS1 denotes the DiBFM with the elements TS1. It should be noted that there is only one source node in QS1 (see Fig. 3(a)) and TS1 (see Fig. 4(a)). The BFM with constant quadrilateral elements is denoted by BFM_QS1, and the BFM with constant triangular elements is denoted by BFM_TS1. The CPU time spent in constructing and solving the system equations is measured to compare the efficiency of the DiBFM and the BFM. The Von Misses stress is observed to study the accuracy and convergence. The relative error is defined

$$error = \frac{1}{|v|_{\max}} \sqrt{\frac{1}{M} \sum_{i=1}^{M} \left[ v_i^{(e)} - v_i^{(n)} \right]^2} \tag{19}$$

where $|v|_{\max}$ is the maximum Von Misses stress over M sampling points, the superscripts $(e)$ and $(n)$ refer to the exact and numerical solutions, respectively.

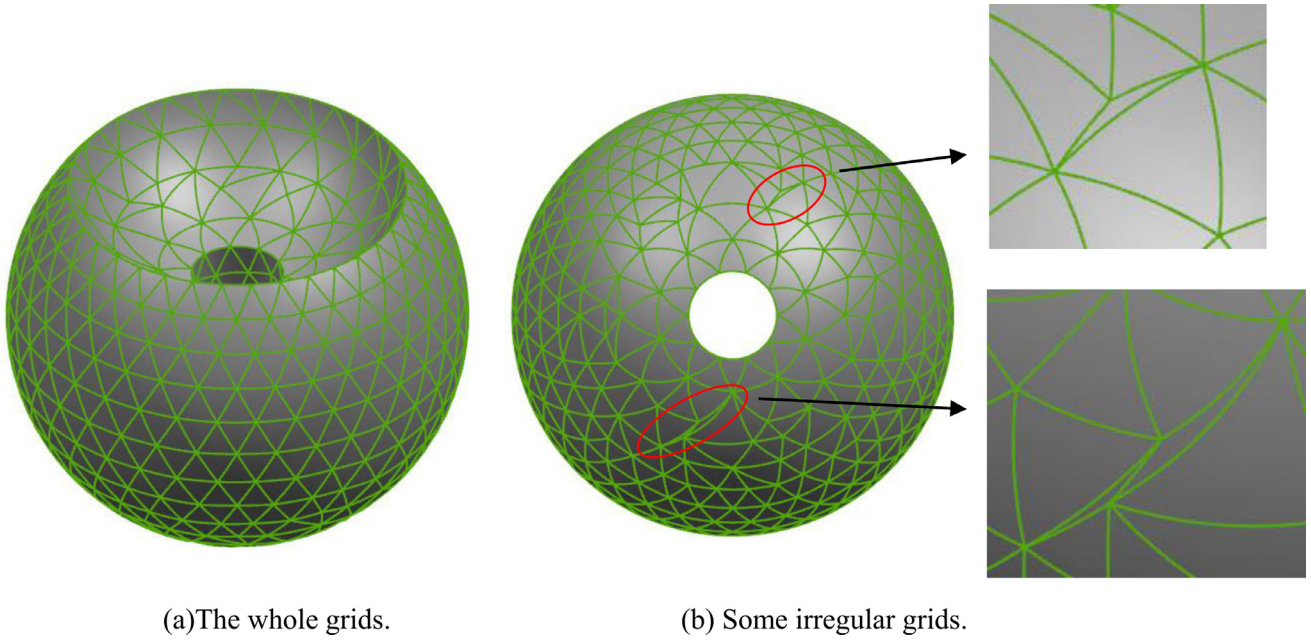


**Fig. 18.** Model discretized by grids.

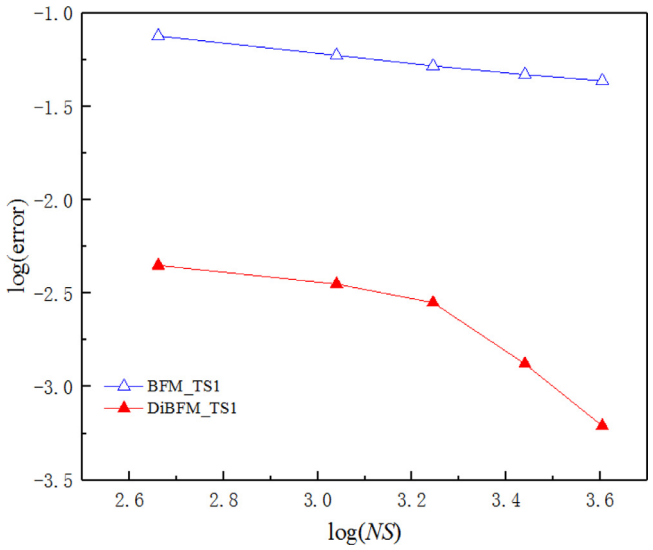


**Fig. 19.** Relative errors of Von Misses stress.

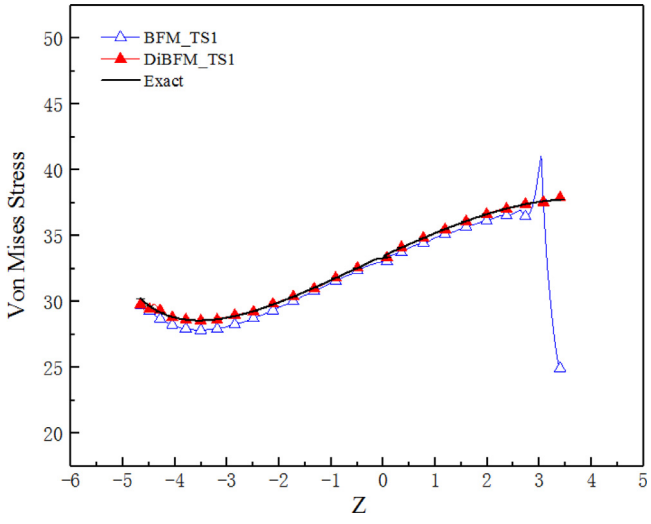


**Fig. 20.** Von Misses stress along the curve AB.

### 5.1. A displacement field problem on a cube

The first example is a*n analytical* displacement field problem on a cube as shown in Fig. 13(a). The Young's modulus $E = 1$ and Poisson's ratio $v = 0.25$. The analytical displacement field imposed on all faces is:

$$\begin{cases} u_x = \left(y^3 - z^3\right) - 3(y - z)x^2 \\ u_y = \left(z^3 - x^3\right) - 3(z - x)y^2 \\ u_z = \left(x^3 - y^3\right) - 3(x - y)z^2 \end{cases}. \tag{20}$$

which satisfy all equilibrium equations. The Von Misses stress is observed to study the accuracy and convergence.

The Analytical displacement field problem on a cube is solved by the BFM_TS1, the BFM_QS1, the DiBFM_TS1 and the DiBFM_QS1 with different number of source nodes (*NS*). The number of sample points in total *M* is 180, and 60 sample points for each the diagonal surface shown in Fig. 13(b). The relative errors of Von Misses stress on total sampling points, and the CPU time spent in constructing and solving the system equations are listed in Tables 2 and 3. For a more intuitive comparison between these two methods, the relative errors of Von Misses stress are plotted in Fig. 14. Combined with the exact solution, the Von Misses stress along a line AB is shown in Fig. 15. These numerical results are obtained by using 600 source nodes. From Figs. 14 and 15, it clearly shows

**Table 2**
Numerical results obtained by the BFM_TS1 and DiBFM_TS1.

| *NS* | BFM_TS1 | | DiBFM_TS1 | |
|---|---|---|---|---|
| | *Error* | *Time(s)* | *Error* | *Time(s)* |
| 84 | 8.85E-02 | 3 | 1.29E-02 | 4 |
| 132 | 7.11E-02 | 3 | 5.00E-03 | 6 |
| 606 | 5.34E-02 | 7 | 9.20E-04 | 25 |
| 1284 | 3.88E-02 | 28 | 3.57E-04 | 97 |
| 2430 | 3.00E-02 | 97 | 1.09E-04 | 340 |

**Table 3**
Numerical results obtained by the BFM_QS1 and DiBFM_QS1.

| *NS* | BFM_QS1 | | DiBFM_QS1 | |
|---|---|---|---|---|
| | *error* | *Time(s)* | *error* | *Time(s)* |
| 96 | 8.31E-02 | 3 | 3.65E-04 | 5 |
| 150 | 7.12E-02 | 3 | 1.96E-04 | 6 |
| 600 | 5.03E-02 | 11 | 4.76E-05 | 38 |
| 1176 | 4.50E-02 | 27 | 3.86E-05 | 125 |
| 2400 | 4.17E-02 | 126 | 3.63E-05 | 452 |

that the DiBFM can obtain more accurate results than the BFM with the same number of source nodes. The CPU time spent in constructing and solving the system equations is illustrated in Fig. 16. This figure shows that for the same CPU time, the DiBFM can achieve a higher accuracy than the BFM. The results in Figs. 14–16 indicate that the DiBFM has much higher accuracy, convergence rates and computational efficiency than the BFM.

#### 5.1.1. A displacement field problem on a trimmed sphere

The second example aims to further verify the accuracy and efficiency of the DiBFM, and show the potential advantages that the DiBFM reduces the requirement of shape regularity for elements.

The second example is a quadratic displacement field problem on a trimmed sphere (see Fig. 17(a)). The radius of the sphere centered at the point C1 is 5, and the sphere is trimmed by a smaller sphere with a radius of 4 and a cylinder with the diameter of 2. The center of the smaller sphere is at the point C2. The size distributions are shown in the axially-symmetrical sectional view of the model (see Fig. 17(b)). The Young's modulus $E = 1$ and Poisson's ratio $\nu = 0.25$. The analytical displacement field imposed on all faces is:

$$\begin{cases} u_x = -2x^2+3y^2+3z^2 \\ u_y = 3x^2-2y^2+3z^2 \\ u_z = 3x^2+3y^2-2z^2 \end{cases}. \tag{21}$$

which satisfy all equilibrium equations.

In order to compare the accuracy and the efficiency of the BFM and DiBFM with elements in "bad" shape, this problem is solved by the BFM_TS1 and the DiBFM_TS1 with totally 458, 1096, 1758, 2756 and 4024 source nodes, respectively. The relative errors of Von Misses stress are evaluated over 200 sample points uniformly distributed along a curve AB (see Fig. 17(c)). The relative errors of Von Misses stress with different number of source nodes are shown in Fig. 19. With 1096 source nodes, the Von Misses stress along the curve AB is plotted in Fig. 20. The discretized results with different number of grids both own some irregular grids (see Fig. 18(b)). And the discretized result with 1096 grids is presented in Fig. 18. As can be seen from Figs. 18–20, even for the very irregular elements, high accuracy can be achieved by the DiBFM. And Fig. 21 illustrates the DiBFM requires less CPU time than the BFM for the same level of accuracy.

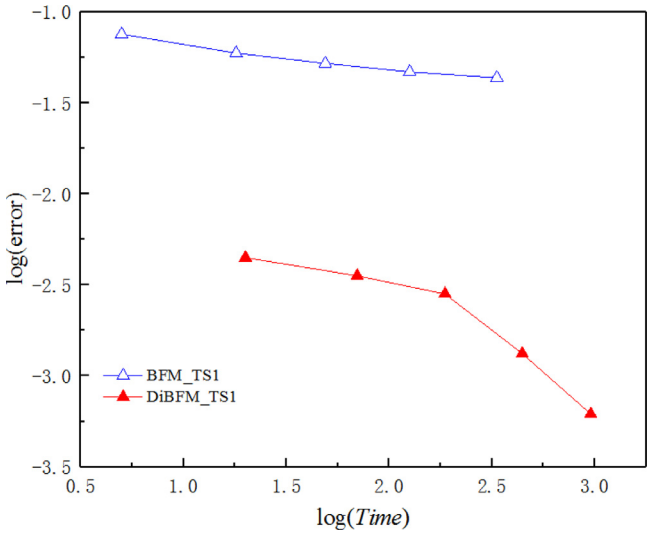


**Fig. 21.** Comparison of computational efficiency for Von Misses stress.

### 5.2. Three-way pipe with a rounded corner

In this example, a three-way pipe with a rounded corner is analyzed to show the capability of DiBFM to solve the problem of the structure as shown in Fig. 22(a). The dimensions of the horizontal hollow cylinder

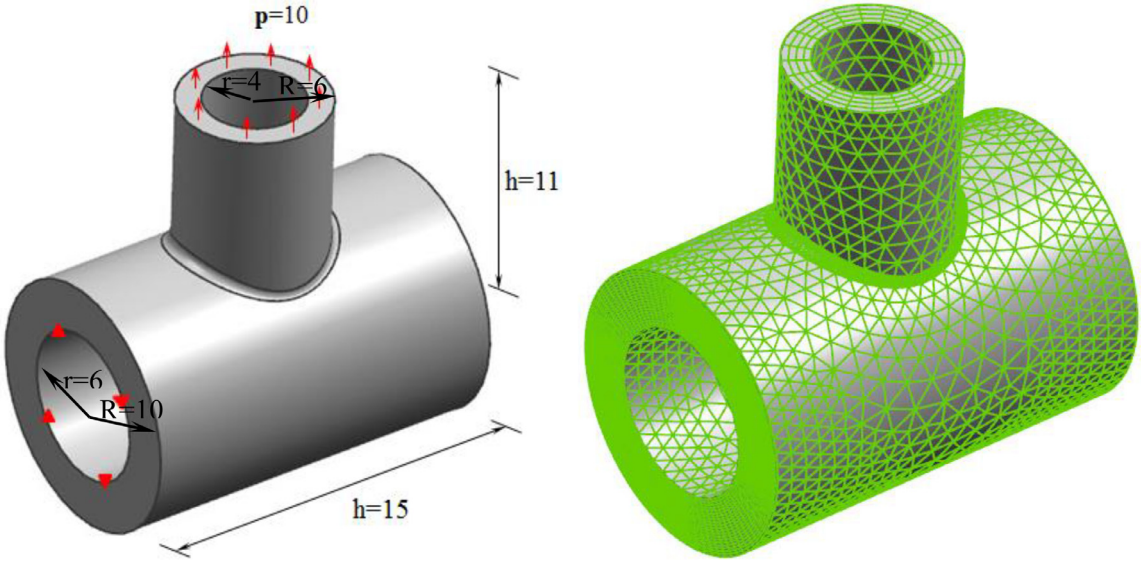


(a) Geometry and boundary conditions (b) Mesh used in DiBFM

**Fig. 22.** Three-way pipe.

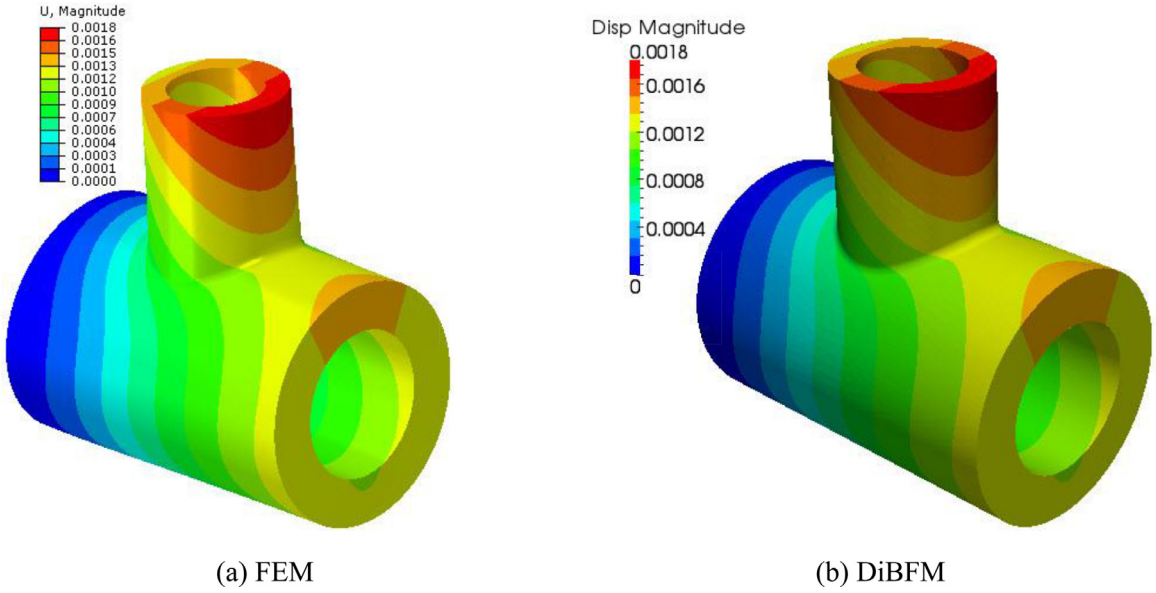


**Fig. 23.** The displacement results of the two methods.

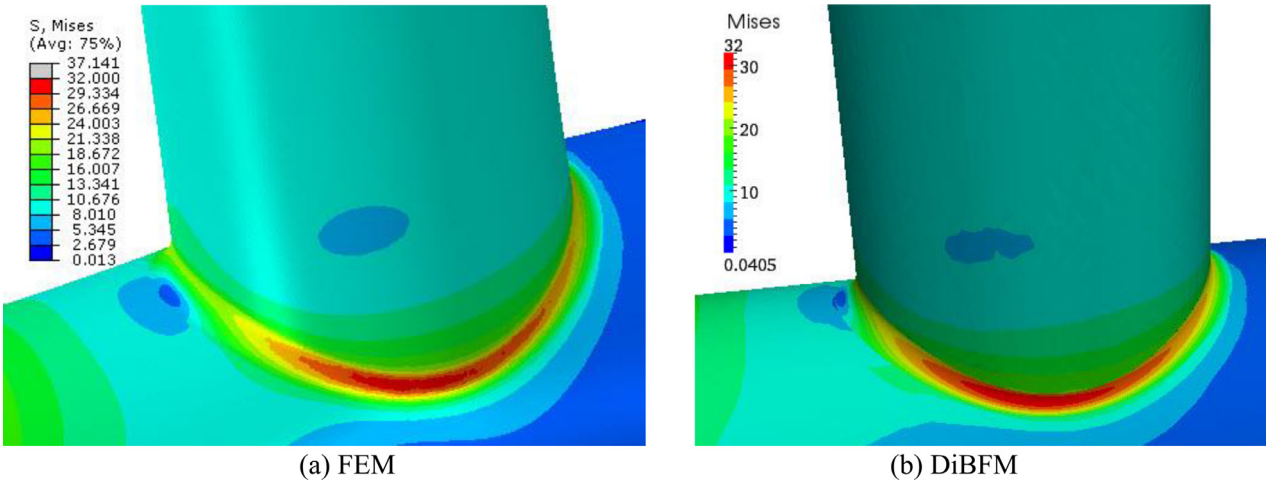


**Fig. 24.** The Von Misses stress at the rounded corner in the two methods.

are selected as $R = 10$, $r = 6$ and $h = 15$ and the dimensions of the vertical hollow cylinder are $R = 6$, $r = 4$ and $h = 11$. In addition, the rounded corner between the two hollow cylinders is $r = 0.4$. In this model, Young's modules $E = 200{,}000$ and Poisson's ratio $\nu = 0.25$. The boundary conditions are specified as: end of the horizontal hollow cylinder is clamped, the top face of the vertical hollow cylinder is subjected to a uniform traction $p = 10$. The number of source nodes in total is 7527 with element mesh shown in Fig. 22(b). The FEM is considered as a reference for comparisons with 1,453,636 nodes. The finite-element analyses are performed through the software ABAQUS, and 3D 4-node tetrahedron elements are employed in the mesh process. It is worth mentioning that the overall computation time consumed by FEM is significantly shorter than that consumed by the DiBFM.

We consider the Von Misses stress on the rounded corner. Since the fixed end is of a sharp corner, the Von Misses stress at this point is not convergent, i.e., when the mesh density increases, the Von Misses stress value at the corner increases. Thus, the Von Misses stress on the rounded corner, where the failure usually occurs, is chosen for comparison. The displacement magnitude and Von Misses stress with two numerical methods are shown in Figs. 23 and 24 for comparison, respectively.

From Fig. 23, it can be seen that the displacement magnitude by DiBFM are almost coincident with that by FEM. Fig. 24 demonstrates the excellent agreement between these two methods with Von Misses stress around the rounded corner. Fig. 25 shows that the distribution of Von Misses stress at the rounded corner is not smooth enough with 493,657 nodes and 928,384 nodes by FEM. Besides, even if 1,453,636 nodes are used, the distribution at the rounded corner is less smooth than that obtained by DiBFM from Fig. 24, which shows that higher accuracy is achieved by DiBFM. In Fig. 24, the less smooth Von Misses stress on the cylinder surface is due to the use of a coarser mesh in DiBFM. In short, the higher accuracy of Von Misses stress distribution at rounded corner in DiBFM illustrates that the DiBFM is more suitable for solving the problem of the structure with small features.

### 5.3. Angle steel

An angle steel model is analyzed in this example to show the capability of the DiBFM to solve the practical problems in engineering. The geometric model and size are shown in Fig. 26(a). In this model, Young's modules $E = 20{,}000$ and Poisson's ratio $\nu = 0.3$. The bottom of the angle steel is fixed and the back of the angle steel is subjected to a uniform pressure $p = 1.0$. The number of source nodes is 6937 with element mesh on the surface shown in Fig. 26(b). In FEM, 1,519,450 nodes with quadratic tetrahedral elements are used based on the finite element software ABAQUS. The displacement magnitude and Von Misses stress are shown in Figs. 27 and 28. The maximum displacement magnitude (U_max) and Von Misses stress (S_max) are presented in Table 4.

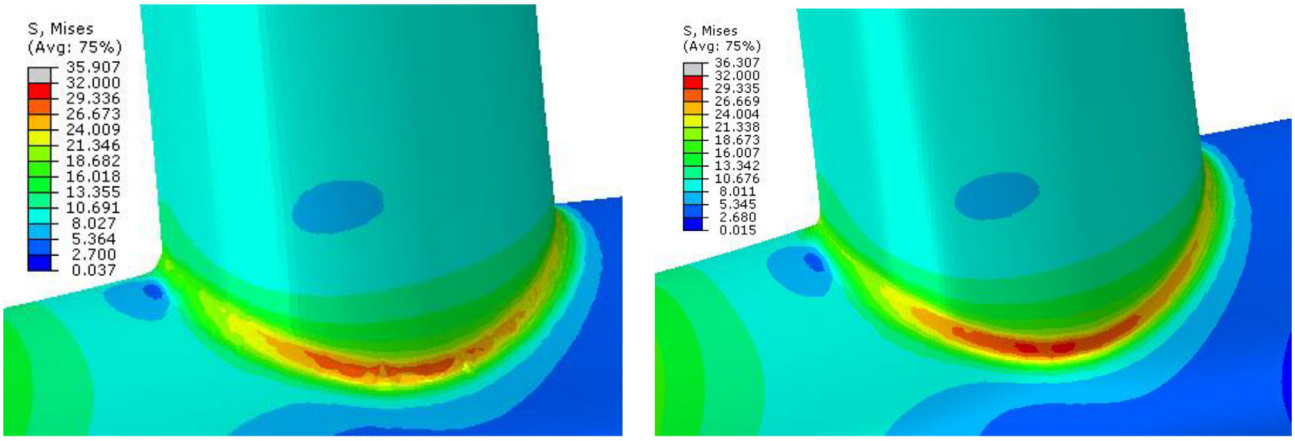


**Fig. 25.** The Von Misses stress at the rounded corner with different numbers of nodes in FEM.

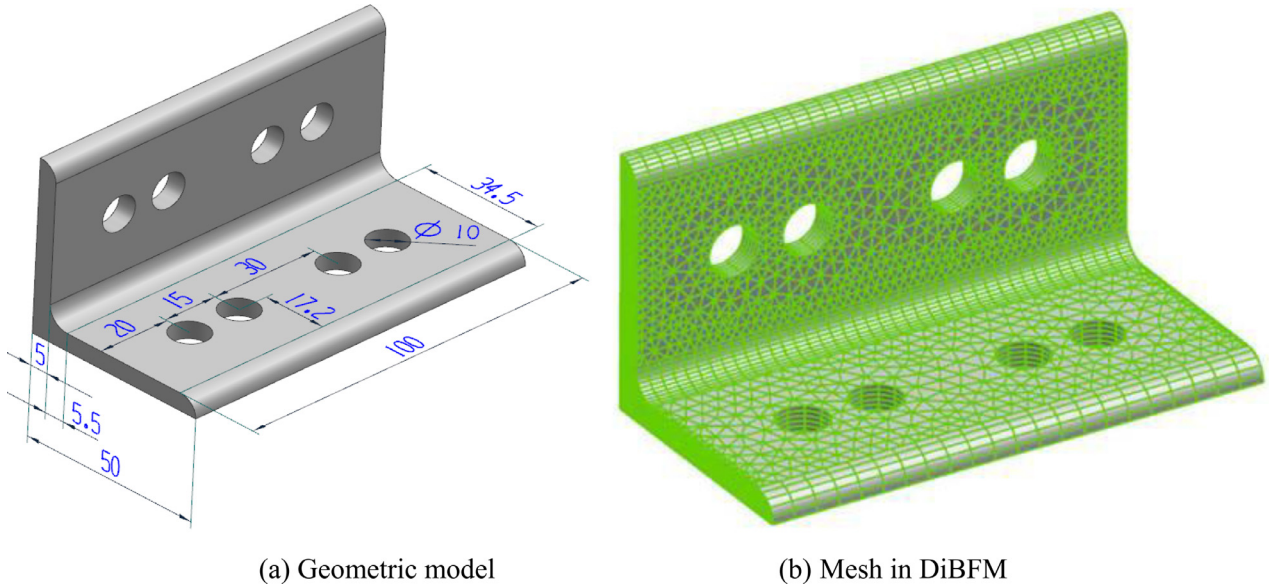


**Fig. 26.** Angle steel.

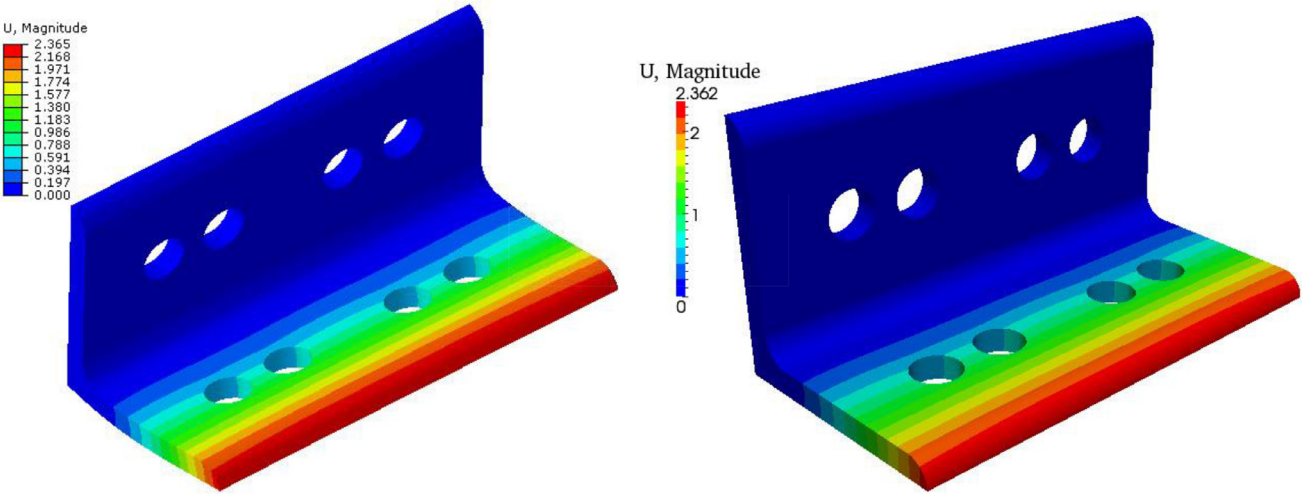


**Fig. 27.** The displacement results by the two methods.

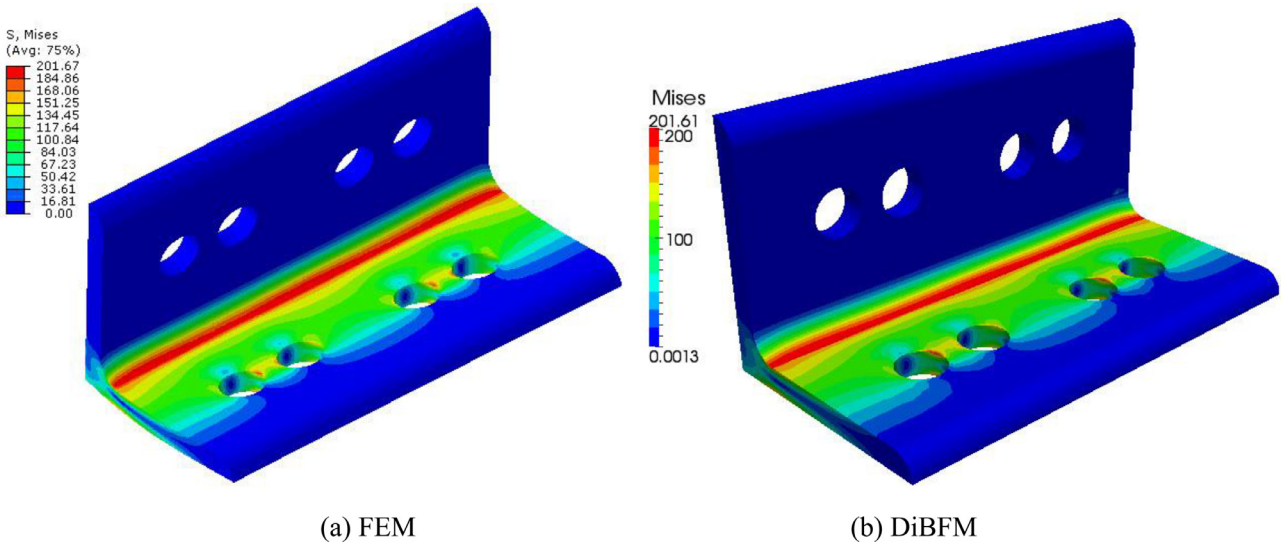


**Fig. 28.** The Von Misses stress results by the two methods.

**Table 4**
Comparison of the maximum displacement magnitude and the maximum Von Misses stress.

| Result | FEM | DiBFM | $err = \lvert \frac{x_{DiBFM} - x_{FEM}}{x_{FEM}} \rvert \times 100\%$ |
|---|---|---|---|
| U_max | 2.365 | 2.362 | 0.127% |
| S_max | 201.67 | 201.61 | 0.030% |

From Figs. 27 and 28, it is hard to see the difference between DiBFM and FEM. In addition, from Table 4, the relative errors of the maximum displacement magnitude and the maximum Von Misses stress are 0.127% and 0.03%, respectively. These results demonstrate that the DiBFM can solve the practical problems in engineering with high accuracy.

## 6. Conclusions

The dual interpolation boundary face method (DiBFM) has been extended to 3D elasticity problems successfully in this paper which is combined with the dual interpolation method and the boundary face method. The numerical results have demonstrated the high degrees of accuracy and convergence in 3D elasticity problems. In addition, the numerical results show that the DiBFM is suitable for solving the problem of structures with small features. This is a very significant behavior, since the maximum Von Misses stress usually occurs at the small features. This behavior will provide more reasonable stress results in numerical analysis. In the future work, the DiBFM will be extended to analyze the large-scale complex structures via combining with the fast multipole method [13] or adaptive cross approximation algorithm [25], and we will apply the DiBFM to analyze a “dirty” geometry model discretized by discontinuous grids.

## Declaration of Competing Interest

None.

## Acknowledgments

This work was supported by National Natural Science Foundation of China under grant number 11772125 and 11472102.

## References

[1] Zhang JM, Lin WC, Dong YQ. A double-layer interpolation method for implementation of BEM analysis of problems in potential theory. Appl Math Model 2017;51:250–69.
[2] Zhang JM, Lin W, Dong Y. A dual interpolation boundary face method for elasticity problems. Eur J Mech A Solids 2019;73:500–11.
[3] Zhang JM, Zhong YD, Dong YQ, Lin WC. Expanding element interpolation method for analysis of thin-walled structures. Eng Anal Bound Elem 2018;86:82–8.
[4] Zhang JM, Shu XM, Trevelyan J, Lin WC, Chai PF. A solution approach for contact problems based on the dual interpolation boundary face method. Appl Math Model 2019;70:643–58.
[5] Zhang JM, Dong YQ, Lin WC, Ju CM. A singular element based on dual interpolation BFM for V-shaped notches. Appl Math Model 2019;71:208–22.
[6] Zhang JM, Chi BT, Lin WC, Ju CM. A dual interpolation boundary face method for three-dimensional potential problems. Int J Heat Mass Transf 2019;140:862–76.
[7] Manolis GD, Banerjee PK. Conforming versus non-conforming boundary elements in three-dimensional elastostatics. Int J Numer Methods Eng 1986;23(10):1885–904.
[8] Grilli ST, Svendsen IA. Corner problems and global accuracy in the boundary element solution of nonlinear wave flows. Eng Anal Bound Elem 1990;7(4):178–95.
[9] Rosen D, Cormack DE. On corner analysis in the BEM by the continuation approach. Eng Anal Bound Elem 1995;16:53–63.
[10] Thompson JF, Soni BK, Weatherill NP. Handbook of grid generation. CRC Press; 1998.
[11] Bern M, Eppstein D, Teng S H. Parallel construction of quadtrees and quality triangulations. Int J Comput Geom Appl 1999;9(06):517–32.
[12] Zhang JM, Qin XY, Han X. A boundary face method for potential problems in three dimensions. Int J Numer Methods Eng 2009;80:320–37.
[13] Liu Y. Fast multipole boundary element method: theory and applications in engineering. Cambridge University Press; 2009.
[14] Simpson RN, Bordas SPA, Trevelyan J, Rabczuk T. A two-dimensional isogeometric boundary element method for elastostatic analysis. Comput Methods Appl Mech Eng 2012;209:87–100.
[15] Politis C, Ginnis AI, Kaklis PD, Belibassakis K, Feurer C. An isogeometric BEM for exterior potential-flow problems in the plane. In: Proceedings of the SIAM/ACM joint conference on geometric and physical modeling. ACM; 2009. p. 349–54.
[16] Takahashi T, Matsumoto T. An application of fast multipole method to isogeometric boundary element method for Laplace equation in two dimensions. Eng Anal Bound Elem 2012;36(12):1766–75.
[17] Chen L, Marburg S, Zhao W, Liu C, Chen H. Implementation of isogeometric fast multipole boundary element methods for 2D half-space acoustic scattering problems with absorbing boundary condition. J Theor Comput Acoust 2019;27(02):1850024.
[18] Qin XY, Zhang JM, Li GY, Sheng XM, Song Q, et al. An element implementation of the boundary face method for 3D potential problems. Eng Anal Bound Elem 2010;34(11):934–43.
[19] Zhang JM, Huang C, Lu CJ, Han L, Wang P, et al. Automatic thermal analysis of gravity dams with fast boundary face method. Eng Anal Bound Elem 2014;41:111–21.
[20] Zhang JM, Ju CM, Divo E, Zhong YD, Chi BT. A binary-tree subdivision method for evaluation of singular integrals in 3D BEM. Eng Anal Bound Elem 2019;103:80–93.
[21] Zienkiewicz OC, Taylor RL, Zhu JZ. The finite element method: its basis and fundamentals. Amsterdam: Elsevier; 2013.

[22] Lancaster P, Salkauskas K. Surface generated by moving least squares methods. Math Comput 1981;37:141–58.
[23] Brebbia CA, Telles JCF, Wrobel LC. Boundary element techniques: theory and applications in engineering. Springer Science & Business Media; 2012.
[24] Press WH, Teukolsky SA, Vetterling WT, Flannery BP. Numerical recipes 3rd edition: the art of scientific computing. Cambridge University Press; 2007.
[25] Bebendorf M. Approximation of boundary element matrices. Numer Math 2000;86(4):565–89.